Intra-Body Optical Channel Modeling for *In Vivo* Wireless Nanosensor Networks

Hongzhi Guo, *Student Member, IEEE*, Pedram Johari, *Student Member, IEEE*, Josep Miquel Jornet, *Member, IEEE*, and Zhi Sun, *Member, IEEE*

***Abstract*—*In vivo* wireless nanosensor networks (iWNSNs) consist of nanosized communicating devices, which can operate inside the human body in real time. iWNSNs are at the basis of transformative healthcare techniques, ranging from intra-body health-monitoring systems to drug-delivery applications. Plasmonic nanoantennas are expected to enable the communication among nanosensors in the near infrared and optical transmission window. This result motivates the analysis of the phenomena affecting the propagation of such electromagnetic (EM) signals inside the human body. In this paper, a channel model for intra-body optical communication among nanosensors is developed. The total path loss is computed by taking into account the absorption from different types of molecules and the scattering by different types of cells. In particular, first, the impact of a single cell on the propagation of an optical wave is analytically obtained, by modeling a cell as a multi-layer sphere with complex permittivity. Then, the impact of having a large number of cells with different properties arranged in layered tissues is analyzed. The analytical channel model is validated by means of electromagnetic simulations and extensive numerical results are provided to understand the behavior of the intra-body optical wireless channel. The result shows that, at optical frequencies, the scattering loss introduced by cells is much larger than the absorption loss from the medium. This result motivates the utilization of the lower frequencies of the near-infrared window for communication in iWNSNs.**

***Index Terms*—Intra-body channel modeling, nanonetworks, plasmonic nanoantenna, wireless nanosensor networks.**

I. Introduction

NANOTECHNOLOGY is enabling the development of novel nanosensors, which are able to detect new types of events at the nanoscale with unprecedented accuracy. *In vivo* nanosensing systems [1], which can operate inside the human body in real time, have been recently proposed as a way to provide faster and more accurate disease diagnosis and treatment than traditional technologies based on *in vitro* medical devices. Unfortunately, the sensing range of each nanosensor is limited to its close nanoenvironment and, thus, many nanosensors are needed to cover significant volumes. Moreover, an external device and the user interaction are necessary to read the actual measurement. By means of communication, nanosensors will be able to autonomously transmit their sensing information in a multi-hop fashion to a common sink, react to instructions from a command center, or coordinate joint actions when needed. The resulting *in vivo* wireless nanosensor networks (iWNSNs) will enable smart health-monitoring and drug-delivery systems, among many others [2].

For the time being, there are several wireless technologies that could enable the communication between nanosensors. Among others, molecular communication, which is based on the exchange of molecules to transmit information, is currently being thoroughly investigated [3]. This mechanism is naturally used by cells to exchange information and coordinate their actions, and could be enabled by means of synthetic biology. However, the very low achievable data rates in molecular communications [4] could drastically limit the usefulness of nanosensor networks. At the same time, information-carrying molecules could result in interference with the naturally-occurring processes to be sensed. Another very relevant technology is the utilization of ultrasonic communication, based on the utilization of very high frequency acoustic waves [5]. However, for the time being, the size and power limitations of ultrasonic acoustic transducers pose a major challenge in their integration with biological nanosensors.

From the electromagnetic (EM) perspective, the miniaturization of a conventional metallic antenna to meet the size requirements of a nanosensor results in very high resonant frequencies, in the order of several hundreds of terahertz (THz or 10^{12} Hz). At such frequencies, metals do not behave as perfect electric conductors, but exhibit a complex conductivity. This enables the propagation of confined electromagnetic modes at the surface of the antenna, which commonly referred to as surface plasmon polariton (SPP) waves. Starting from this phenomenon, novel plasmonic nanoantennas for wireless communication among nanodevices have been recently proposed. Among others, in [6], [7], the concept of graphene-based plasmonic nanoantennas for terahertz-band (0.1–10 THz) communication was first introduced. Similarly, in [8], [9], the concept of plasmonic nanoantennas for near infrared and optical frequencies based on noble metals and metamaterials is thoroughly discussed.

The possibility to wirelessly interconnect nanosensors deployed inside and over the human body using plasmonic nanoantennas enables many bio-nanosensing applications but, at the same time, introduces multiple challenges. For example, the propagation of THz-band waves inside the human body is drastically impacted by the absorption of liquid water molecules [10], [11]. THz-band radiation is not ionizing, i.e., it cannot damage the molecular structure of any biological entity. However, it can induce internal vibrations in different types of molecules, including liquid water molecules. The friction resulting from this vibration generates heat, which could eventually result in biological tissue damage due to thermal effects. Alternatively, it

Manuscript received August 30, 2015; revised November 02, 2015; accepted November 27, 2015. Date of publication December 11, 2015; date of current version February 26, 2016. This work was supported by the U.S. National Science Foundation (NSF) under Grant No. CBET-1445934. *Asterisk indicates corresponding author.*

H. Guo, P. Johari, and J. M. Jornet are with the Department of Electrical Engineering, University at Buffalo, the State University of New York, Buffalo, NY 14260 USA (e-mail: hongzhig@buffalo.edu; pedramjo@buffalo.edu; jmjornet@buffalo.edu; zhisun@buffalo.edu).

*Z. Sun is with the Department of Electrical Engineering, University at Buffalo, the State University of New York, Buffalo, NY 14260 USA (e-mail: hongzhig@buffalo.edu; pedramjo@buffalo.edu; jmjornet@buffalo.edu; zhisun@buffalo.edu).

Color versions of one or more of the figures in this paper are available online at http://ieeexplore.ieee.org.

Digital Object Identifier 10.1109/TNB.2015.2508042

1536-1241 © 2015 IEEE. Personal use is permitted, but republication/redistribution requires IEEE permission.
See http://www.ieee.org/publications_standards/publications/rights/index.html for more information.

is well known that the absorption from liquid water molecules is minimal in the so-called optical window, roughly between 400 THz and 750 THz [12]. In fact, plasmonic nanodevices at optical frequencies have already been utilized in several *in vivo* applications [13], [14].

Motivated by this result, we advocate for the use of the optical window for intra-body wireless communication among nanosensors with plasmonic nanoantennas. Besides water, however, there are multiple phenomena that affect the intra-body propagation of EM waves, which cannot be captured with traditional channel models for lower frequency communication. For example, in classical channel models, the human body is modeled as a layered material with different permeabilities and permittivities [15]. However, from the nanosensor perspective, the body is a collection of different types of elements, such as cells, organelles, proteins, and molecules, with different geometry and arrangement as well as different electromagnetic properties. While the optical properties of some of these elements have been broadly analyzed [16]–[18], these studies are mostly valid only when a large area (in terms of the wavelength) is illuminated. Unfortunately, this is not the case when plasmonic nanoantennas are utilized.

In this paper, we develop a channel model for intra-body optical communication in iWNSNs. In particular, we derive a mathematical framework to compute the channel path loss by taking into account the absorption from different types of molecules and the scattering by different types of cells. First, we analyze the impact of a single cell on the propagation of an optical wave generated by an electric nanodipole. For this, we model a cell as a multi-layer sphere with different complex permittivities. The scattered field coefficients are derived and a new T-matrix for the multi-layer cell is found. After that, several important properties of the cell is discussed, such as forward scattering, absorption cross section and scattering cross section, among others. Then, we analyze the impact of having a very large number of cells with different electromagnetic properties arranged in layered tissues. Based on the characteristics of the cell, a simplified multiple scattering model is applied to find the electric field intensity. Finally, the channel performance in terms of path loss is discussed.

The reminder of this paper is organized as follows. The details on the single cell analytical model are provided in Section II. Numerical results are then provided to understand the impact of different biological entities on the signal propagation. Next, the multiple scattering model is developed and validated in Section III. After that, the intra-body channel path loss derivation and channel performance analysis are provided in Section IV. Finally, this paper is concluded in Section V.

II. Radiation Source and Single Cell Model

For our frequency range of interest, i.e., the near-infrared and optical transmission window, the wavelength is in the order of several hundred nanometers. As a result, on the one hand, the impact of molecules, proteins, and other nanometric entities is well captured by global or macroscopic magnitudes, such as the complex permittivity, which results in the well-known absorption loss [16]–[18]. However, on the other hand, the impact of relatively large entities, such as different types of cells, needs special consideration. Compared to existing works on optical signal propagation in biological tissues [16]–[18], the illumination area from a single nanoantenna is much smaller than that of an external macroscopic laser. Therefore, we need to take into account the impact of individual cells. In this section, we first investigate the influence of a single cell on the propagation of an optical wave radiated by an electric nanodipole [9], [19]. Then, the developed model is validated by FEM simulation and electromagnetic properties of a cell are discussed.

A. Spherical Wave Expansion of Plasmonic Nanoantenna

The radiation source is an optical plasmonic nanoantenna, which is modeled as an electric dipole [8]. The radiated electromagnetic fields by the antenna can be written as [20],

$$\begin{cases} \mathbf{e}_r = \frac{\eta I_0 l \cos\theta}{2\pi r^2}\left[1+\frac{1}{jkr}\right]e^{-jkr}\hat{r}; \\ \mathbf{e}_\theta = \frac{j\eta k I_0 l \sin\theta}{4\pi r}\left[1+\frac{1}{jkr}-\frac{1}{(kr)^2}\right]e^{-jkr}\hat{\theta}; \mathbf{e}_\phi = 0; \\ \mathbf{h}_\phi = \frac{jkI_0 l\sin\theta}{4\pi r}\left[1+\frac{1}{jkr}\right]e^{-jkr}\hat{\phi}; \mathbf{h}_r = 0; \mathbf{h}_\theta = 0, \end{cases} \quad (1)$$

where I_0 is the input current, l is the antenna length, $\eta = \sqrt{\mu/\epsilon}$, μ is the permeability, ϵ is the permittivity, $k = \omega\sqrt{\mu\epsilon}$, ω is the angular frequency, $j = \sqrt{-1}$, and r is the distance from the origin. Time-dependent $e^{j\omega t}$ is assumed in this paper. The radiated fields by an electric dipole antenna is TM_{01} mode which can also be expressed in vector spherical wave functions (VSWFs). By using the spherical wave expansion in the Appendix, (1) can be rewritten as,

$$\begin{aligned} \mathbf{E}_a(o_a,\mathbf{r}) &= -\frac{\omega\mu I_0 l k}{4\pi}\mathbf{n}^3_{01}(o_a,\mathbf{r}) \\ &= \underbrace{-\frac{\omega\mu I_0 l k}{4\pi}\boldsymbol{\mathcal{I}}}_{\text{coefficients}}\begin{bmatrix}\mathbf{M}^3_{mn}(o_a,\mathbf{r}) \\ \mathbf{N}^3_{mn}(o_a,\mathbf{r})\end{bmatrix} \\ &= \mathbf{E}_a\begin{bmatrix}\mathbf{M}^3_{mn}(o_a,\mathbf{r}) \\ \mathbf{N}^3_{mn}(o_a,\mathbf{r})\end{bmatrix}, \end{aligned} \quad (2)$$

where n is from 1 to infinity, m is from $-n$ to n, N_{stop} is the maximum value of the order n and the way to find the optimal N_{stop} will be discussed in next subsection, $\mathbf{M}^3_{mn}(o_a,\mathbf{r})$ is expressed in (3), at the bottom of the page, where T stands for transpose, $(o_a,\mathbf{r})$ denotes that o_a is the origin of the spherical coordinates, and $\mathbf{r}$ is the radial vector from the origin o_a to a point. For instance, in Fig. 1, we have two sets of spherical coordinate system: for the antenna, o_a is the origin; for the cell, o_c is the origin. To denote an observation point o_b, we can either use $(o_c,\mathbf{r})$, where $\mathbf{r} = o_b - o_c$, or $(o_a,\mathbf{r})$, where $\mathbf{r} = o_b - o_a$. By substituting $\mathbf{m}^3_{mn}(o_a,\mathbf{r})$ with $\mathbf{n}^3_{mn}(o_a,\mathbf{r})$ in (3), we can obtain the expression of $\mathbf{N}^3_{mn}(o_a,\mathbf{r})$. Note that $\mathbf{n}^3_{01}(o_a,\mathbf{r})$ is a row vector with three elements: $[\mathbf{e}_r, \mathbf{e}_\theta, \mathbf{e}_\phi]$. Since $\mathbf{M}^3_{mn}(o_a,\mathbf{r})$ and $\mathbf{N}^3_{mn}(o_a,\mathbf{r})$ are only determined by the coordinates, if in the same coordinate system, in mathematical deductions we can neglect them and only keep the coefficients $(\mathbf{E}_a)$. The superscript 3 in

$$\mathbf{M}^3_{mn}(o_a,\mathbf{r}) = \left[\underbrace{\mathbf{m}^3_{-11}(o_a,\mathbf{r})^T}_{1^{st}}, \underbrace{\mathbf{m}^3_{01}(o_a,\mathbf{r})^T}_{2^{nd}}, \cdots, \underbrace{\mathbf{m}^3_{mn}(o_a,\mathbf{r})^T}_{[(n+1)^2-n+m-1]^{th}}, \cdots \underbrace{\mathbf{m}^3_{N_{stop}N_{stop}}(o_a,\mathbf{r})^T}_{[(N_{stop}+1)^2-1]^{th}}\right]^T, \quad (3)$$

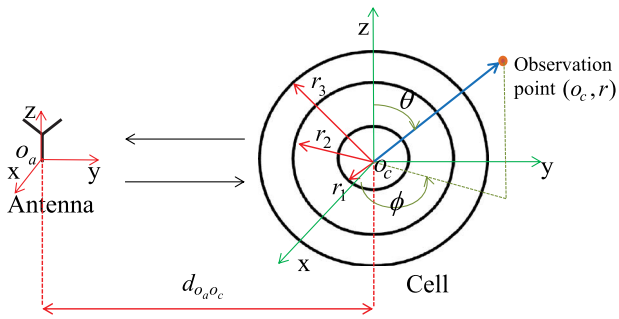

Fig. 1. Illustration of the dipole antenna and spherical cell with three layers.

$\mathbf{N}^3_{mn}(o_a, \mathbf{r})$ and $\mathbf{M}^3_{mn}(o_a, \mathbf{r})$ stands for the traveling wave radiated from the antenna, and $\boldsymbol{\mathcal{I}}$ is a row vector with $2(N_{stop}+1)^2-2$ elements, where the $[(N_{stop}+1)^2+1]^{th}$ element is 1 and all other elements are 0.

B. Single Cell Model

In this part, we look at the impact of a single cell on the wave propagation. The cell is modeled as a spherical shell (the cell membrane) filled with cytoplasm. Although the spherical-cell model is widely used in biomedical research [16]–[18]], the shape of the cell is not necessarily spherical and the position of its nucleus may not be the cell center [21]. In this paper, we consider the simplified spherical cell model to provide a tractable and analytical solution to focus on more critical intra-body channel parameters, including size, density, and complex permittivity of each type of cells as well as the surrounding medium.

According to classical scattering theory, the scattered field by a sphere can be derived by using Mie scattering theory [22]. The scattered field can be expressed by the product of T-matrix $\mathcal{T}$ and the incident field $\mathbf{E}_{in}$, i.e., $\mathbf{E}^T_{sca} = \mathcal{T} \cdot \mathbf{E}^T_{in}$. However, since we consider the cell is multi-layer, the conventional T-matrix, which only considers a single layer sphere, does not work here. Thus, the T-matrix should be rederived. Firstly, we express the antenna radiated field in the cell's spherical coordinate. Then, considering it as the incident field, we find the scattered field by enforcing boundary conditions. As a result, the T-matrix can be derived.

1) Incident Field: Equation (2) is formulated in the coordinate whose origin o_a is the center of the antenna. When we derive the T-matrix for a sphere, we should move the origin to the center of the sphere o_c. The translational addition theorem for vector spherical wave functions [23] is utilized to do so. According to [23], [24],

$$\mathbf{M}^3_{mn}(o_a, \mathbf{r}) = \mathbf{A}^3_{mn}\mathbf{M}^1_{mn}(o_c, \mathbf{r}) + \mathbf{B}^3_{mn}\mathbf{N}^1_{mn}(o_c, \mathbf{r}); \tag{4a}$$

$$\mathbf{N}^3_{mn}(o_a, \mathbf{r}) = \mathbf{A}^3_{mn}\mathbf{N}^1_{mn}(o_c, \mathbf{r}) + \mathbf{B}^3_{mn}\mathbf{M}^1_{mn}(o_c, \mathbf{r}); \tag{4b}$$

where $\mathbf{A}^3_{mn}$ and $\mathbf{B}^3_{mn}$ are translational matrices with dimension $[(N_{stop}+1)^2-1] \times [(N_{stop}+1)^2-1]$, N_{stop} is related to $kd_{o_a o_c}$, where $d_{o_a o_c}$ is the distance between o_a and o_c. If $kd_{o_a o_c}$ is large, we have to use higher N_{stop} to maintain the accuracy [25]. The detailed expression for $\mathbf{A}^3_{mn}$ and $\mathbf{B}^3_{mn}$ can be found by referring to [24]. Ideally, n should be from 1 to infinity to exactly express the field at a point. However, due to the high computation burden, we have to truncate n at a certain order where the result can converge to the precise value. N_{stop} can be approximated by $kd_{o_a o_c}$. In this paper, the cell size is around 2 times larger than the wavelength and the distance between cells and the antenna can be several thousands of wavelength. As a result, a large truncation order N_{stop} should be applied.

In our scattering model, we define that the near region is where we can use the exact model to calculate the radiated field, and the far region is where we consider the radiated field from the antenna (scatter) is a plane wave. The exact model using translational addition theorem considers all the modes of the wave. On the contrary, by considering the propagating wave in the far region is a plane wave, we reduce the mode number by eliminating some unimportant modes. The longer the distance between the source and the scatter, the fewer dominant modes. In this way, the computation burden can be significantly reduced. The boundary between the near region and far region is set as a variable d_t. If we need high accuracy, the boundary should be far away from the source. In contrast, if we want to sacrifice the accuracy to reduce the computation time, this boundary can be relatively close to the antenna.

a) Near region transform: In order to make our analysis more succinct, (4) can be written in matrix form, which is

$$\begin{bmatrix} \mathbf{M}^3_{mn}(o_a, \mathbf{r}) \\ \mathbf{N}^3_{mn}(o_a, \mathbf{r}) \end{bmatrix} = \begin{bmatrix} \mathbf{A}^3_{mn} & \mathbf{B}^3_{mn} \\ \mathbf{B}^3_{mn} & \mathbf{A}^3_{mn} \end{bmatrix} \begin{bmatrix} \mathbf{M}^1_{mn}(o_c, \mathbf{r}) \\ \mathbf{N}^1_{mn}(o_c, \mathbf{r}) \end{bmatrix} = \mathbf{H}_{o_a \to o_c} \begin{bmatrix} \mathbf{M}^1_{mn}(o_c, \mathbf{r}) \\ \mathbf{N}^1_{mn}(o_c, \mathbf{r}) \end{bmatrix} \tag{5}$$

where the matrix $\mathbf{H}_{o_a \to o_c}$ consists of the translational coefficients. Note that the left most item in (5) is the same as the right most item in (2). Therefore, (2) can be rewritten as

$$\mathbf{E}_a(o_a, \mathbf{r}) = -\frac{\omega\mu I_0 lk}{4\pi} \boldsymbol{\mathcal{I}} \mathbf{H}_{o_a \to o_c} \begin{bmatrix} \mathbf{M}^1_{mn}(o_c, \mathbf{r}) \\ \mathbf{N}^1_{mn}(o_c, \mathbf{r}) \end{bmatrix}. \tag{6}$$

In this way, we formally transform the radiated spherical wave from the antenna's coordinate (origin o_a) to a cell's coordinate (origin o_c).

b) Far region transform: Intuitively, the wave in front of the spherical wave in the far field can be regarded as a plane wave. Both $\mathbf{M}^3_{nm}(o_c, \mathbf{r})$ and $\mathbf{N}^3_{nm}(o_c, \mathbf{r})$ consist of the second kind of spherical Hankel function $h^2_n(kr)$ (see Appendix). In the far field, $h^2_n(kr) \simeq (j)^{n+1}e^{-jkr}/kr$. If kr is large, within a small range (much smaller than r) the spherical wave can be regarded as a plane wave. Suppose that the distance between the antenna and a cell is larger than the threshold distance d_t and the incoming wave can be regarded as a plane wave. The electric field at the center of a cell can be calculated by using (2). Then we can obtain the magnitude of the electric field and decompose it into Cartesian coordinates, i.e., $\mathbf{E}_a(o_a, \mathbf{r}) = E_x\hat{x} + E_y\hat{y} + E_z\hat{z}$, where the origin of the Cartesian coordinates is the center of the cell.

Once we have the magnitude of the plane wave, the next step is to find the propagation direction of the equivalent plane wave. The direction is perpendicular to the plane formed by electric field and magnetic field. The direction of the electric field $(\hat{e})$ can be found from (2), while the magnetic field is linked with electric field by Maxwell equations.

Finally, the direction of the plane wave is $\hat{k}_{in} = \sin\theta_{in}\cos\phi_{in}\hat{x} + \sin\theta_{in}\sin\phi_{in}\hat{y} + \cos\theta_{in}\hat{z}$, where θ_{in} and ϕ_{in} denote the direction of the incoming wave. By rearranging the plane wave's expression in [22], we can obtain

$$\mathbf{E}_a(o_a, \mathbf{r}) = [E_{\theta_{in}}, E_{\phi_{in}}][\mathbf{C}_{mn}(\theta_{in}, \phi_{in}), \mathbf{D}_{mn}(\theta_{in}, \phi_{in})] \begin{bmatrix} \mathbf{M}^1_{nm}(o_c, \mathbf{r}) \\ \mathbf{N}^1_{nm}(o_c, \mathbf{r}) \end{bmatrix}; \tag{7}$$

where $E_{\theta_{in}}$ and $E_{\phi_{in}}$ are the components of E_{in} in direction $\hat{\theta_{in}}$ and $\hat{\phi_{in}}$; the dimension of $\mathbf{C}_{mn}(\theta_{in}, \phi_{in})$ and $\mathbf{D}_{mn}(\theta_{in}, \phi_{in})$ is

$(N_{stop}+1)^2-1$ columns and 2 rows, and a column with order (m,n) can be written as

$$\mathbf{C}_{mn}(\theta_{in},\phi_{in}) = \frac{(-1)^m j^n(2n+1)}{n(n+1)}\begin{bmatrix}\frac{-jm}{\sin\theta_{in}}P_n^{-m}(\cos\theta_{in})e^{-jm\phi_{in}}\\ \frac{-d}{d\theta_{in}}P_n^{-m}(\cos\theta_{in})e^{-jm\phi_{in}}\end{bmatrix} \quad (8)$$

$$\mathbf{D}_{mn}(\theta_{in},\phi_{in}) = \frac{(-1)^m j^n(2n+1)}{n(n+1)}\begin{bmatrix}\frac{-jd}{d\theta_{in}}P_n^{-m}(\cos\theta_{in})e^{-jm\phi_{in}}\\ \frac{-m}{\sin\theta_{in}}P_n^{-m}(\cos\theta_{in})e^{-jm\phi_{in}}\end{bmatrix} \quad (9)$$

2) T-Matrix for Single Sphere: By taking a close look at (6) and (7), we can find that both the near region and far region expressions have the same right most item which is only determined by the cell's spherical coordinate. All other items can be regarded as coefficients which are determined by the relative position of the cell and the antenna. Therefore, when deriving the T-matrix, we can consider the near region's and far region's incoming field have the same format but different coefficients. The spherical cell shown in Fig. 1 is considered as a typical red blood cell, which consists of three layers: the first layer corresponds to the cytoplasm in cell with complex permittivity ϵ_1 and radius r_1; the second layer is the hemoglobin with permittivity ϵ_2 and radius r_2; and the third layer is the cell membrane (primarily fat) with permittivity ϵ_3 and radius r_3. The propagation medium surrounding the cells is the intercell cytoplasm with permittivity ϵ_4. Since biological cells are not magnetic, the permeability of the cell and the medium are set as the same as vacuum which is μ_0 [26]. Therefore, the corresponding wavenumbers k_1, k_2, k_3 and k_4 are solely determined by the complex permittivity of each layer and the propagation medium.

Generally, the solution to Maxwell equations in spherical structure are the spherical Bessel function, spherical Neumann function, and spherical Hankel function. The former two functions can represent standing waves and the last one can denote propagating waves. Also, due to the singularity of spherical Neumann functions, at the origin of the coordinates, the standing waves can only be expressed by spherical Bessel functions. Thus, the electric fields in each layer of the cell (center is o_c) are summarized as follows:

$$\mathbf{E}_{l1}(o_c,\mathbf{r}) = [\boldsymbol{\mathcal{A}}_M \quad \boldsymbol{\mathcal{A}}_N]\begin{bmatrix}\mathbf{M}^1_{mn}(o_c,\mathbf{r})\\ \mathbf{N}^1_{mn}(o_c,\mathbf{r})\end{bmatrix} \quad (10a)$$

$$\mathbf{E}_{l2}(o_c,\mathbf{r}) = [\boldsymbol{\mathcal{B}}_M \quad \boldsymbol{\mathcal{B}}_N]\begin{bmatrix}\mathbf{M}^1_{mn}(o_c,\mathbf{r})\\ \mathbf{N}^1_{mn}(o_c,\mathbf{r})\end{bmatrix} + [\boldsymbol{\mathcal{C}}_M \quad \boldsymbol{\mathcal{C}}_N]\begin{bmatrix}\mathbf{M}^2_{mn}(o_c,\mathbf{r})\\ \mathbf{N}^2_{mn}(o_c,\mathbf{r})\end{bmatrix} \quad (10b)$$

$$\mathbf{E}_{l3}(o_c,\mathbf{r}) = [\boldsymbol{\mathcal{D}}_M \quad \boldsymbol{\mathcal{D}}_N]\begin{bmatrix}\mathbf{M}^1_{mn}(o_c,\mathbf{r})\\ \mathbf{N}^1_{mn}(o_c,\mathbf{r})\end{bmatrix} + [\boldsymbol{\mathcal{E}}_M \quad \boldsymbol{\mathcal{E}}_N]\begin{bmatrix}\mathbf{M}^2_{mn}(o_c,\mathbf{r})\\ \mathbf{N}^2_{mn}(o_c,\mathbf{r})\end{bmatrix} \quad (10c)$$

$$\mathbf{E}_{sca}(o_c,\mathbf{r}) = [\boldsymbol{\mathcal{F}}_M \quad \boldsymbol{\mathcal{F}}_N]\begin{bmatrix}\mathbf{M}^3_{mn}(o_c,\mathbf{r})\\ \mathbf{N}^3_{mn}(o_c,\mathbf{r})\end{bmatrix}, \quad (10d)$$

where $\mathbf{E}_{li}$ stands for the electric field in the ith layer and $\mathbf{E}_{sca}$ is the scattered electric field. The row vectors from $\mathcal{A}_M$ to $\mathcal{F}_N$ contains the unknown coefficients for the wave functions which need to be found by enforcing boundary conditions. The dimension of each unknown vector is $(N_{stop}+1)^2-1$.

For a cell we have 3 boundaries and 12 unknown vectors. The T-matrix is formed by $\mathcal{F}_M$ and $\mathcal{F}_N$. We can find the unknown coefficients by enforcing boundary conditions which are the continuity of $\hat{r}\times\mathbf{E}$ and $\hat{r}\times\nabla\times\mathbf{E}$ [22]. Specifically, on each boundary, we need to guarantee the continuity of $\mathbf{M}_{mn}(o_c,\mathbf{r})$ and $\mathbf{N}_{mn}(o_c,\mathbf{r})$ for both electric field and magnetic field. As a result, we have 4 equations for each boundary and totally 12 equations to find those unknown vectors.

Fortunately, the electric field expansion in (10) can be further simplified since it can be written in a general form: $E = f(r)f(\theta)f(\phi)$, where $f(r)$ is the spherical Bessel, Neumman, or Hankel functions, which depends on the layer, $f(\theta)$ is the associated Legendre function, and $f(\phi)$ is $e^{jm\phi}$. Due to the symmetrical structure of the sphere, for a point on a boundary, $f(\theta)$ and $f(\phi)$ are the same in the two layers. As a result, the boundary conditions are only determined by $f(r)$. Referring to Appendix, the spherical Bessel, Neumman, or Hankel functions are only determined by order n. Therefore, only order n is considered when calculating the unknown coefficients. Since n is from 1 to N_{stop}, we have $12N_{stop}$ equations for boundary conditions.

After balancing the boundary conditions, we can obtain the equation for the nth order

$$\boldsymbol{\mathcal{S}}^n_{cell}\cdot\boldsymbol{\mathcal{U}}^n = \mathfrak{I}^n, \quad (11)$$

where $\boldsymbol{\mathcal{S}}^n_{cell}$ is the matrix provided at the bottom of the next page, $\boldsymbol{\mathcal{U}}^n$ is the nth order unknown coefficients whose transpose is shown in an equation at the bottom of the next page, and $\mathfrak{I}^n$ is the incident field. It should be noted that $\boldsymbol{\mathcal{S}}^n_{cell}$ is only determined by the cell. For a spherical function $[b_n(x)]^* = b_n(x) + x\cdot b'_n(x)$, where the prime symbol denotes derivative.

According to our previous discussion, the incident field $\mathfrak{I}^n$ can be expressed in a general way. Here we remove the coefficients and keep the spherical vectors. In other words, the magnitude of the incident field has been normalized, i.e., only $\mathbf{M}^1_{nm}(o_c,\mathbf{r})$ and $\mathbf{N}^1_{nm}(o_c,\mathbf{r})$ are considered and their coefficients are normalized as 1. In the end, the removed coefficients will be multiplied with the T-matrix to find the scattering coefficients. As a result, the transpose of $\mathfrak{I}^n$ can be written as

$$\mathfrak{I}^{n\,T} = \{j_n(k_4r_3),[j_n(k_4r_3)]^*,[j_n(k_4r_3)]^*,j_n(k_4r_3), 0,0,0,0,0,0,0,0\}. \quad (14)$$

Based on $\mathfrak{I}^n$, $\boldsymbol{\mathcal{S}}^n_{cell}$, and (11), we use Gaussian elimination to find the unknown coefficients U^n from $n=1$ to $n=N_{stop}$. We cannot use the inverse of $\boldsymbol{\mathcal{S}}^n_{cell}$ to find the unknown coefficients, since this matrix is almost singular (the value of spherical Hankel function is much larger than that of spherical Bessel function). Once we have $\boldsymbol{\mathcal{F}}_M$ and $\boldsymbol{\mathcal{F}}_N$, the T-matrix can be written as

$$\boldsymbol{\mathcal{T}} = diag(\boldsymbol{\mathcal{F}}_M,\boldsymbol{\mathcal{F}}_N). \quad (15)$$

$\boldsymbol{\mathcal{T}}$ is a diagonal block matrix with dimension $2(N_{stop}+1)^2-2$.

3) Single Sphere Model: Consider the scenario illustrated in Fig. 1, the electric field at any point outside of the cell can be written as

$$\mathbf{E}_t = \mathbf{E}_a(o_a,\mathbf{r}) + \mathbf{E}_{sca}(o_c,\mathbf{r}) = -\frac{\omega\mu I_0 lk}{4\pi}\boldsymbol{\mathcal{I}}\begin{bmatrix}\mathbf{M}^3_{mn}(o_a,\mathbf{r})\\ \mathbf{N}^3_{mn}(o_a,\mathbf{r})\end{bmatrix} + \begin{cases}\left\{\boldsymbol{\mathcal{T}}\left[-\frac{\omega\mu I_0 lk}{4\pi}\boldsymbol{\mathcal{I}}\mathbf{H}_{o_a\to o_c}\right]^T\right\}^T\begin{bmatrix}\mathbf{M}^3_{mn}(o_c,\mathbf{r})\\ \mathbf{N}^3_{mn}(o_c,\mathbf{r})\end{bmatrix}, \\ \quad when\ d_{o_ao_c}<d_t \\ \left\{\boldsymbol{\mathcal{T}}\{[E_{\theta_{in}},E_{\phi_{in}}][\mathbf{C}_{mn}(\theta_{in},\phi_{in}),\mathbf{D}_{mn}(\theta_{in},\phi_{in})]\}^T\right\}^T \\ \quad\times\begin{bmatrix}\mathbf{M}^3_{mn}(o,\mathbf{r})\\ \mathbf{N}^3_{mn}(o,\mathbf{r})\end{bmatrix},\ when\ d_{o_ao_c}\geq d_t.\end{cases} \quad (16)$$

where $d_{o_ao_c}$ is the distance between o_a and o_c. Note that in (16), since the expression for antenna and cell are in different coordi-

TABLE I
RELATIVE PERMITTIVITY VS WAVELENGTH [12], [27], [28]

λ(nm)	cytoplasm	fat	hemoglobin
450	$1.79 - j2.73 \cdot 10^{-9}$	$2.13 - j6.68 \cdot 10^{-7}$	$2.04 - j3.46 \cdot 10^{-3}$
500	$1.78 - j2.68 \cdot 10^{-9}$	$2.13 - j2.20 \cdot 10^{-7}$	$2.03 - j1.26 \cdot 10^{-3}$
550	$1.78 - j5.22 \cdot 10^{-9}$	$2.13 - j9.89 \cdot 10^{-8}$	$2.01 - j2.86 \cdot 10^{-3}$
600	$1.77 - j2.87 \cdot 10^{-8}$	$2.13 - j6.47 \cdot 10^{-8}$	$1.99 - j2.50 \cdot 10^{-4}$
650	$1.77 - j4.37 \cdot 10^{-8}$	$2.13 - j7.12 \cdot 10^{-8}$	$1.99 - j2.87 \cdot 10^{-5}$
700	$1.77 - j8.88 \cdot 10^{-8}$	$2.13 - j5.26 \cdot 10^{-8}$	$1.99 - j2.43 \cdot 10^{-5}$
750	$1.77 - j4.15 \cdot 10^{-7}$	$2.13 - j1.70 \cdot 10^{-7}$	$1.99 - j4.68 \cdot 10^{-5}$
800	$1.77 - j3.33 \cdot 10^{-7}$	$2.13 - j7.45 \cdot 10^{-8}$	$1.99 - j7.83 \cdot 10^{-5}$
850	$1.77 - j7.81 \cdot 10^{-7}$	$2.13 - j1.26 \cdot 10^{-7}$	$1.99 - j1.08 \cdot 10^{-4}$
900	$1.76 - j1.29 \cdot 10^{-6}$	$2.13 - j9.66 \cdot 10^{-7}$	$1.99 - j1.29 \cdot 10^{-4}$
950	$1.76 - j7.69 \cdot 10^{-6}$	$2.13 - j8.69 \cdot 10^{-7}$	$1.99 - j1.37 \cdot 10^{-4}$
1000	$1.76 - j7.67 \cdot 10^{-6}$	$2.13 - j6.17 \cdot 10^{-7}$	$1.99 - j1.23 \cdot 10^{-4}$

nates, their vector spherical wave functions are different. In other words, vectors $\hat{r}$, $\hat{\theta}$ and $\hat{\phi}$ are different directions in the two coordinates. Therefore, we cannot simply add together the spherical vector wave functions. In this paper, we first convert the results into the same Cartesian coordinates, whose origin is the observation point, then sum them up. The same method is applied in the following analysis.

C. Numerical Analysis

In this subsection, the theoretical model is validated by using COMSOL Multiphysis. The parameters utilized in FEM simulation is the same as those in theoretical model. Despite the model is general, we particularize it for the specific case of having a nanosensor transmits to another nanosensor inside a blood vessel. The blood vessel is modeled as a medium containing cytoplasm and red blood cells. Since the propagation medium is dispersive, with different frequency, the relative permittivity are different for cytoplasm, fat, and hemoglobin. The detailed wavelength and corresponding permittivity are provided in Table I. Also, in order to model the inhomogeneous environment inside vessel, we consider three different sizes since cells may change their size due to biochemical process. The detailed sizes are presented in Table II, and the superscripts s, m, and l stand for small size, medium size, and large size, respectively. Note that, in order to reduce the computation burden, we consider relatively smaller size than real red blood cells.

TABLE II
SIMULATION PARAMETERS

variable	value	variable	value
ϵ_0	$8.854 \cdot 10^{-12}$ F/m	μ_0	$4\pi \cdot 10^{-7}$ H/m
a	450 nm	r_1^s	$0.87a$
r_2^s	$0.99a$	r_3^s	a
r_1^m	$1.32a$	r_2^m	$1.5a$
r_3^m	$1.58a$	r_1^l	$1.74a$
r_2^l	$1.98a$	r_3^l	$2a$

1) FEM Simulation: In simulation, the distance between the antenna and the cell is set as $1.5a + r_3^m$. In the numerical calculation, we set N_{stop} as 30. The antenna is considered to be a unit dipole, i.e., $I_0 l = 1$, where I_0 is the input current and l is the antenna length. The single cell simulation model in COMSOL Multiphysics is displayed in Fig. 2. The cell is located at the center of the simulation space which is enclosed by a perfect matched layer (PML). The PML is utilized to mimic the infinite environment and its thickness is half wavelength. The simulation in Fig. 2 is conducted with wavelength 450 nm and the cell is medium size. In the following, without specified notation, we use the medium size for the cell. In the numerical analysis, the wavelength is set as 450 nm, 500 nm, 800 nm, and 850 nm and the field intensity is provided in Fig. 3. The x axis is measured in scale a (450 nm) in order to show the dimension more clearly. The electric field is calculated along y-axis from the antenna to the observation point. The developed model agrees with the FEM simulation which proofs that the model is accurate enough. Note that, 450 nm has larger field intensity than 850 nm in Fig. 3. The radiated power by a dipole antenna can be written as $P_{rad} = (\pi\eta/3)|I_0 l/\lambda|^2$. Hence, since we provide them the same dipole moment, the shorter wavelength has larger radiated power, which results in a strong field intensity. In order to make a more fair comparison, we provide them the same radiated power and plot the field intensity in Fig. 4. As we can see, in between the cell and the antenna, the curves are overlapped and after the cell, 450 nm has relatively smaller electric field intensity when compared with the field intensity in Fig. 3.

2) Effect of Cell Position: In order to show the effects of observation point, the total electric field intensity after the cell is computed. The wavelength is continually increased from 450

$$\begin{bmatrix}
-h_n^2(k_4r_3) & 0 & j_n(k_3r_3)y_n(k_3r_3) & 0 & 0 & 0 & 0 & 0 & 0 & 0 & 0 \\
0 & -\left[h_n^2(k_4r_3)\right]^* & 0 & 0 & [j_n(k_3r_3)]^* \frac{k_4}{k_3} & y_n(k_3r_3)]^* \frac{k_4}{k_3} & 0 & 0 & 0 & 0 & 0 & 0 \\
-\left[h_n^2(k_4r_3)\right]^* & 0 & [j_n(k_3r_3)]^* & [y_n(k_3r_3)]^* & 0 & 0 & 0 & 0 & 0 & 0 & 0 & 0 \\
0 & -h_n^2(k_4r_3) & 0 & 0 & j_n(k_3r_3)\frac{k_3}{k_4} & y_n(k_3r_3)\frac{k_3}{k_4} & 0 & 0 & 0 & 0 & 0 & 0 \\
0 & 0 & j_n(k_3r_2) & y_n(k_3r_2) & 0 & 0 & -j_n(k_2r_2) & -y_n(k_2r_2) & 0 & 0 & 0 & 0 \\
0 & 0 & 0 & 0 & [j_n(k_3r_2)]^* & [y_n(k_3r_2)]^* & 0 & 0 & [j_n(k_2r_2)]^* \frac{-k_3}{k_2} & y_n(k_2r_2)]^* \frac{-k_3}{k_2} & 0 & 0 \\
0 & 0 & [j_n(k_3r_2)]^* & [y_n(k_3r_2)]^* & 0 & 0 & -[j_n(k_2r_2)]^* & [y_n(k_2r_2)]^* & 0 & 0 & 0 & 0 \\
0 & 0 & 0 & 0 & j_n(k_3r_2) & y_n(k_3r_2) & 0 & 0 & j_n(k_2r_2)\frac{-k_2}{k_3} & y_n(k_2r_2)\frac{-k_2}{k_3} & 0 & 0 \\
0 & 0 & 0 & 0 & 0 & 0 & j_n(k_2r_1) & y_n(k_2r_1) & 0 & 0 & j_n(k_1r_1) & 0 \\
0 & 0 & 0 & 0 & 0 & 0 & 0 & 0 & [j_n(k_2r_1)]^* & [y_n(k_2r_1)]^* & 0 & [j_n(k_1r_1)]^* \frac{-k_2}{k_1} \\
0 & 0 & 0 & 0 & 0 & 0 & [j_n(k_2r_1)]^* & [y_n(k_2r_1)]^* & 0 & 0 & -[j_n(k_1r_1)]^* & 0 \\
0 & 0 & 0 & 0 & 0 & 0 & 0 & 0 & j_n(k_2r_1) & y_n(k_2r_1) & 0 & j_n(k_1r_1)\frac{-k_1}{k_2}
\end{bmatrix} \tag{12}$$

$$\boldsymbol{\mathcal{U}}^{nT} = [\boldsymbol{\mathcal{A}}_M^n, \boldsymbol{\mathcal{A}}_N^n, \boldsymbol{\mathcal{B}}_M^n, \boldsymbol{\mathcal{B}}_N^n, \boldsymbol{\mathcal{C}}_M^n, \boldsymbol{\mathcal{C}}_N^n, \boldsymbol{\mathcal{D}}_M^n, \boldsymbol{\mathcal{D}}_N^n, \boldsymbol{\mathcal{E}}_M^n, \boldsymbol{\mathcal{E}}_N^n, \boldsymbol{\mathcal{F}}_M^n, \boldsymbol{\mathcal{F}}_N^n]\,; \tag{13}$$

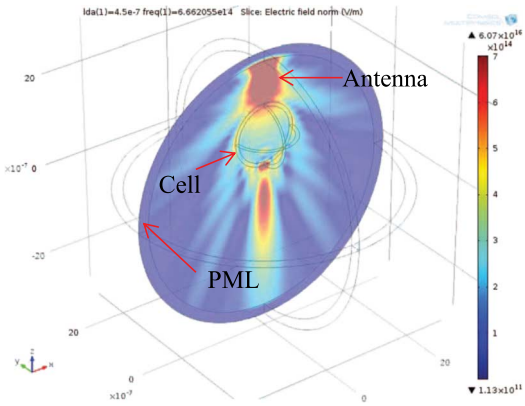

Fig. 2. Electric field intensity (V/m) of single cell: COMSOL Multiphysics simulation model.

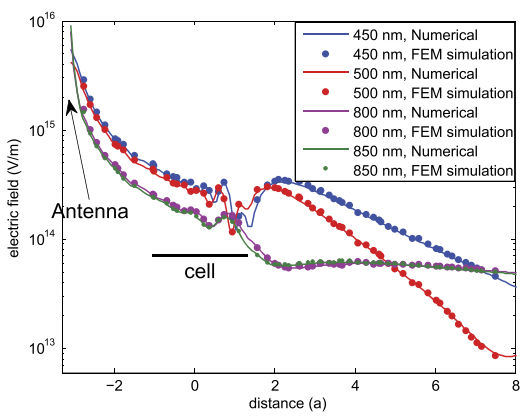

Fig. 3. Field intensity (V/m) for antenna and single cell (same dipole moment). x = 0 is the center of the cell.

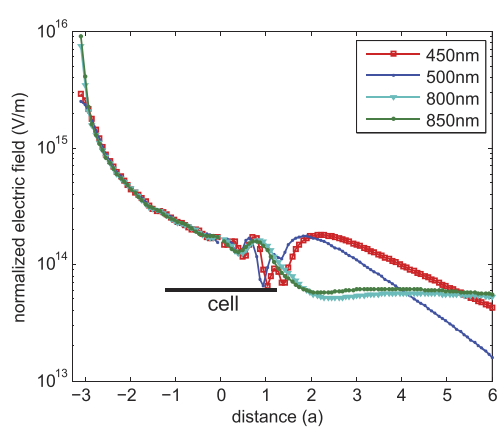

Fig. 4. Normalized field intensity (V/m) for antenna and single cell (same radiation power). x = 0 is the center of the cell.

nm to 1000 nm, i.e., the optical window. The antenna and cell configuration is still the same as that in Fig. 3 and we use the same dipole moment for all the wavelength. In Fig. 5, the observation point is gradually moved from $d = 1.5r_3^m$ to $d = 4.5r_3^m$ on the y-axis in Fig. 1, where d is the distance to the center of the cell. The results can be interpreted from two aspects: 1) for long wavelength, i.e., 700 nm to 1000 nm, since the cell size is relatively small when compared with the wavelength, the scatter has relatively weak influence on field propagation which results in small fluctuation on field magnitude. Therefore, the scattered field is not strong and the dominant field is still from the antenna; 2) for short wavelength, i.e., 450 nm to 650 nm, the size of the

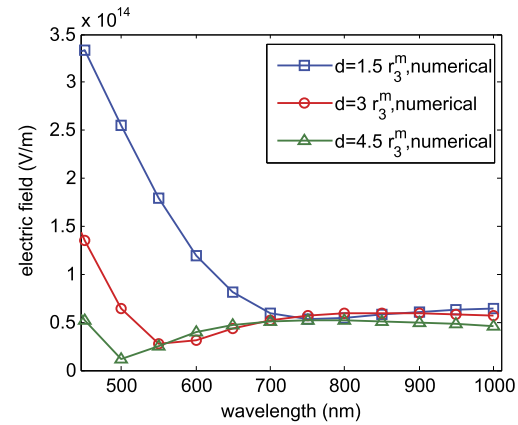

Fig. 5. Impact of observation point on field intensity (V/m).

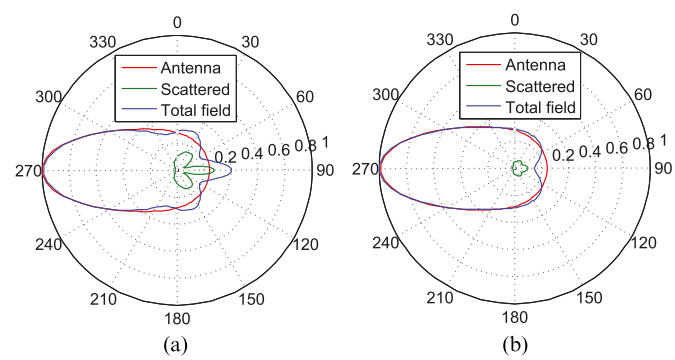

Fig. 6. Polar plot of field intensity, distance from cell center is $1.2r_3^m$. (a) 450 nm; (b) 850 nm.

cell is relatively large for the propagating field. Thus, the electric field suffers from high scattering and the cell can greatly affect the field propagation. If we change the observation point, the field magnitude has high fluctuations. Another interesting finding is that the short wavelength field decreases much faster than the long wavelength field after the cell. The reason can be attributed to the forward scattering which can significantly change the field intensity. When $d = 1.5r_3^m$, the big drop at 500 nm for large cell is due to the strong scattering. As the distance of the observation point increases, this fluctuation disappears.

3) Forward Scattering: Referring to Fig. 2, below the cell there is a strong field region. In order to elucidate the physics better, we consider the electric field separately, i.e., the total field consists of the antenna radiated field and the scattered field from a cell. The electric field intensity is calculated on y-z plane in Fig. 1 from $\theta = 0$ to $\theta = 2\pi$ with $d_{o_a o_c} = 1.5a + r_3^m$. As shown in Fig. 1, the antenna is located on the left side of the cell ($\phi = 1.5\pi$). We define the positive y-axis ($\phi = \pi/2$) as the forward direction. Without loss of generality, we consider the short wavelength is 450 nm and long wavelength is 850 nm. Also, the electric field is normalized by the largest total field intensity, i.e., the maximum field intensity in each figure is normalized to be 1, in order to show the relation better. As depicted in Fig. 6, most of the electric fields are forwardly scattered. Also, behind the cell, the total field is almost the same as the field radiated from antenna which means the cell does not affect the electric field intensity behind it. On the contrary, the forward scattered field has either strong constructive or destructive impacts on the field intensity.

In addition, according to Henyey-Greenstein Phase Function [30] $p(\theta) = (1/4\pi)((1-g^2)/(1+g^2-2g\cos\theta)^{3/2}$, where $g \approx 0.88$ for the considered cells, $\theta = 0$ is the forward direction,

and $p(\theta)$ denotes the amount of photons travel in θ direction, when $\theta = 0$ this function has the maximum value, i.e., forward scattering. Referring back to Figs. 3 and 4, at the end of the cell there are fluctuations, which are due to the forward scattering. On one hand, the radiated field by the antenna decays gradually. On the other hand, the forward scattering greatly increases the field intensity at the end of the cell. Thus, there is a region in between where the field intensity is small. Outside the cell, first the scattered field intensity is dominant. After that, the radiated field from the antenna becomes significant. Therefore, there is a transition which also causes fluctuations.

4) Effect of Cell Size: In Fig. 7, the effect of cell's size is investigated. The same as the discussion for medium size cell in Fig. 5, the small size and large size cells are considered and the observation point is changed continuously from $1.5r_3^m$ to $4.5r_3^m$ along y-axis from the center of the cell. For the large cell, there is strong fluctuation on field magnitude for all the wavelengths. While for small cell, the magnitude is more stable. The same as previous discussion, for the large cell, the wavelength is smaller when compared with the cell size. Hence, for the considered frequency band, the field suffers from high scattering. For the small cell, since the wavelength is relatively larger than its size, therefore, the scattering does not have strong impact.

5) Cross Sections: In order to provide more insights, we calculate the scattering and absorption cross sections of the considered cell with small, medium and large size. According to [22], the normalized scattering cross section can be expressed as

$$Q_s = \frac{\sigma_s}{\sigma_g} = \frac{2}{(k_4 r_3)^2} \sum_{n=1}^{N_{stop}} (2n+1) \left(|\mathcal{F}_M^n|^2 + |\mathcal{F}_N^n|^2 \right), \quad (17)$$

and the normalized extinction cross section is

$$Q_e = \frac{\sigma_e}{\sigma_g} = \frac{-2}{(k_4 r_3)^2} \sum_{n=1}^{N_{stop}} (2n+1) \Re \left(\mathcal{F}_M^n + \mathcal{F}_N^n \right), \quad (18)$$

where σ_s is the scattering cross section, σ_e is the extinction cross section, $\sigma_g = \pi {r_3}^2$ is the geometry cross section, and $\Re$ denotes the real part of a complex number. Note that there is a negative sign for Q_e, since we use the second kind of spherical Hankel function instead of the first kind. The normalized absorption cross section can be written as $Q_a = Q_e - Q_s$. The scattering and absorption cross sections are plotted in Fig. 8. Observe that the scattering cross section is decreasing as the wavelength increases, which agrees with previous discussions. Also, we find that the absorption cross section has a minimum value around 700 nm and it agrees with the absorption of hemoglobin as shown in Fig. 9, which occupies large space in a cell and has large conductivity. Moreover, the larger size of the cell, the larger absorption and scattering cross sections.

In order to validate our results, we compare with the scattering coefficient μ_s and absorption coefficient μ_a for whole blood reported in [29]. The relation between the scattering and absorption coefficients and the corresponding cross sections can be written as [31] $\mu_{s/a} = (N_0/V_0)\sigma_{s/a}$, where N_0 is the number of cells in volume V_0. Therefore, $\mu_{s/a}$ and $\sigma_{s/a}$ are linearly related. As shown in Figs. 8 and 9, the absorption coefficient and scattering coefficients agree with the corresponding cross sections. However, there are still some differences due to the shape, size, materials, biochemical effects, among others.

III. Multi-Cell Model

In this section, the effects of multi-cell scattering on EM field propagation are discussed. Due to the large numbers of cells and their relatively large size, we have limited computation capability. Hence, the discussion is divided into two parts. One focuses on depth and the other one focuses on breadth. For the depth model, we consider the cells are aligned on a chain. For the breadth model, we consider there are multiple cells on a plane and several planes form a three dimensional lattice.

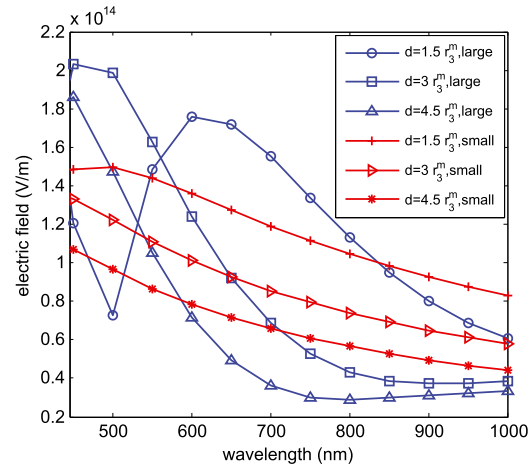

Fig. 7. Effect of cell's size.

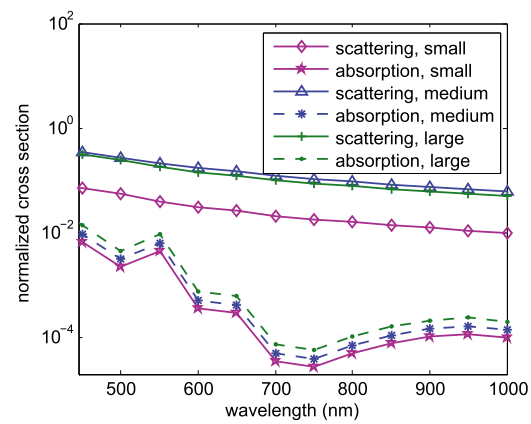

Fig. 8. Scattering and absorption cross sections for one cell with small, medium, and large size.

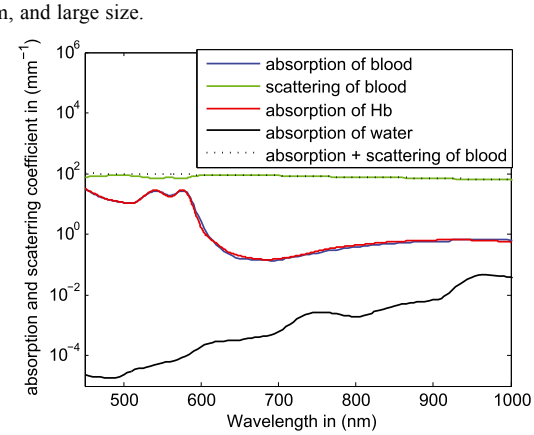

Fig. 9. Scattering and absorption coefficients (mm^{-1}) for whole blood [29]. Hb stands for hemoglobin.

A. Chain Model

In this model, the long distance field propagation is considered. As depicted in Fig. 10, N cells $(c_1, c_2, \cdots, c_l, \cdots, c_N)$ are placed along a line with mutual interval d_i. The distance between the antenna and the first cell is $d_{o_a o_{c1}}$. Due to multiple

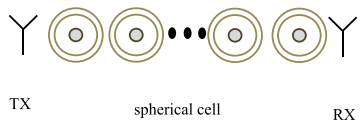

Fig. 10. Illustration of a chain of spherical cells.

scattering, the incident field on a cell c_l consists of the field from the antenna and the fields scattered from all other cells. Note that those scatters can be regarded as an antenna (radiation source) and the aforementioned approach for single cell can be directly applied by using the scattered field coefficients instead of the antenna's coefficients. Therefore, the scattered field from cell c_l can be written as

$$\mathbf{E}_{sca}^{l} = \left\{ \boldsymbol{\mathcal{T}} \left(\sum_{i=1, i\neq l}^{N} \left(\mathbf{E}_{sca}^{i} \mathbf{H}_{o_{ci}\to o_{cl}} \right) + \mathbf{E}_a \mathbf{H}_{o_a \to o_{cl}} \right)^T \right\}^T . \tag{19}$$

In (19), the origin of the coordinate is cell c_l's center. We only keep the scattering coefficients and the VSWFs are neglected to simplify the analysis.

In (19), $\mathbf{H}_{o_{ci}/o_a \to o_{cl}}$ is determined by the relative positions and $\mathbf{E}_a$ is determined by the antenna. Thus, only $\{\mathbf{E}_{sca}^{i}, i = 1, 2, \cdots, N\}$ are to be identified. We can write N such equations and solve them simultaneously. In the previous section, we observe that the scattered field from a cell is mostly forward. Hence, only the forwardly scattered field is considered on this chain and (19) can be simplified as

$$\mathbf{E}_{sca}^{l} = \left\{ \boldsymbol{\mathcal{T}} \left(\sum_{i=1}^{l-1} \left(\mathbf{E}_{sca}^{i} \mathbf{H}_{o_{ci}\to o_{cl}} \right) + \mathbf{E}_a \mathbf{H}_{o_a \to o_{cl}} \right)^T \right\}^T . \tag{20}$$

Furthermore, if the distance between the source and the scatter is longer than d_t (threshold between near region and far region), the incoming field for the scatter is regarded as a plane wave. Therefore, (20) can be further developed as

$$\mathbf{E}_{sca}^{l} = \left\{ \boldsymbol{\mathcal{T}} \left(\sum_{i=0}^{N-M} \left[E_{\theta_i}, E_{\phi_i} \right] \left[\mathbf{C}_{mn}(\theta_i, \phi_i), \mathbf{D}_{mn}(\theta_i, \phi_i) \right] + \sum_{i=l-M,}^{l-1} \mathbf{E}_{sca}^{i} \mathbf{H}_{o_{ci}\to o_{cl}} \right)^T \right\}^T , \tag{21}$$

where $\mathbf{E}_{sca}^{0}$ is the radiated field from antenna, M is the number of cells within d_t, and θ_i and ϕ_i are the incoming angles of the scattered field from cell c_i. Once the scattered field coefficients are determined for each cell, the electric field at any point can be calculated by adding together all the scattered fields and the radiated field from the antenna,

$$\mathbf{E_t} = \mathbf{E}_a(o_a, \mathbf{r}) + \sum_{i=1}^{N} \mathbf{E}_{sca}(o_{ci}, \mathbf{r}). \tag{22}$$

B. Chain Model Validation

The developed model is validated by using COMSOL Multiphysics. Due to the limitation of the software's computation capability, we consider N is three and measure the electric field intensity along the axis of the chain. $d_{o_a o_{c1}}$ is set as $1.5a + r_3^m$ and d_{int} is $5a$. Without loss of generality, the wavelength is set as 450 nm. Also, d_t is $15a$ which means all the three cells and the antenna are considered as in the near region of each other. As shown in Fig. 11, the developed models matches well with

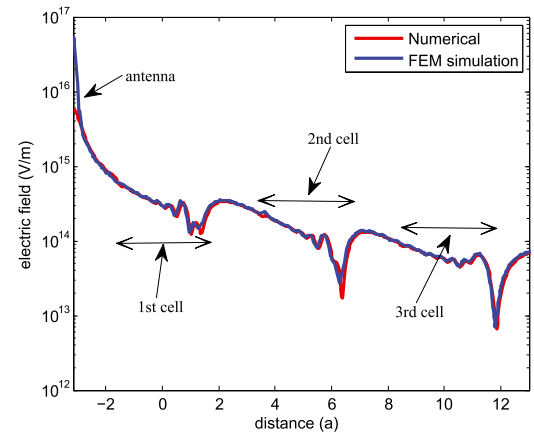

Fig. 11. Electric field intensity distribution for three cells along the chain.

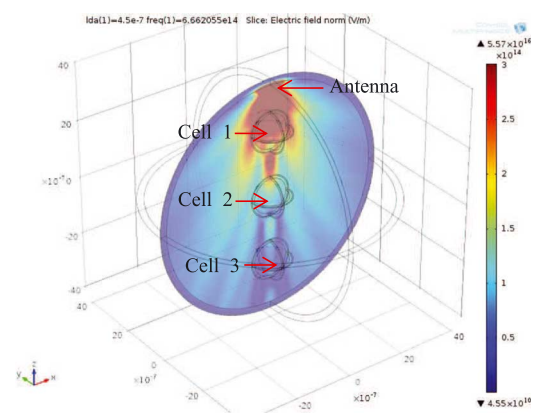

Fig. 12. Electric field intensity (V/m) of chain model, FEM simulation in COMSOL Multiphysics.

the FEM simulation. More importantly, even the backward scattered field is neglected here, we can see the developed model is still accurate enough when compared with the full-wave simulation. Thus, the assumption in the previous section is validated here. Also, a more straightforward illustration of the scattered field intensity on the 2D plane that contains the cells is shown in Fig. 12. As we can see after each cell, the strongest scattered field is around the forward direction which can also validate our assumption. In addition, since we use an approximation in the far region, we set d_t as $10a$ which means if the distance between two cells are larger than $10a$ the wave is regarded as a plane wave. As a result, the radiated field by the antenna is considered as a plane wave for the third cell. The proposed method is evaluated in Fig. 13. We can see some fluctuations inside the third cell due to some neglected modes in the plane wave. However, outside the cell, the approximation is still accurate enough. Since the prerequisite of the assumption is that the cell is far from the scattering source, we can foresee that as the distance increases, the fluctuations will become smaller and smaller.

C. Three Dimensional Lattice Model

The three-dimensional lattice model consists of N_p planes and each plane has N_r rows and N_c columns, as shown in Fig. 14. The horizontal interval d_h, vertical interval d_v and the interval between two planes d_p are the same which are set as $5a$. Note that several planes can form a layer and different layers may have different kinds of cells. To make the model more realistic, the odd number rows's x coordinates are $0.5d_h$ larger than those of the even number rows. The size of the cell is medium which was provided in Table II. The cells are labeled from left bottom to right

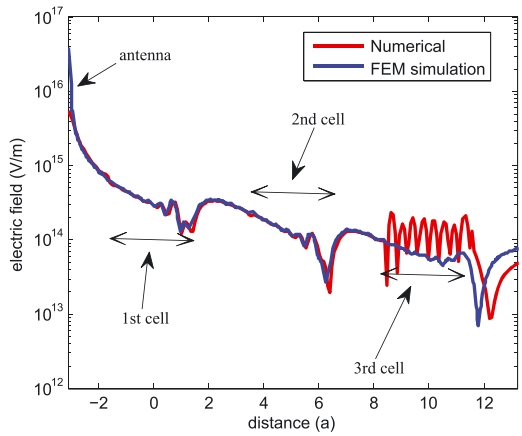

Fig. 13. Electric field intensity distribution for three cells with plane wave approximation.

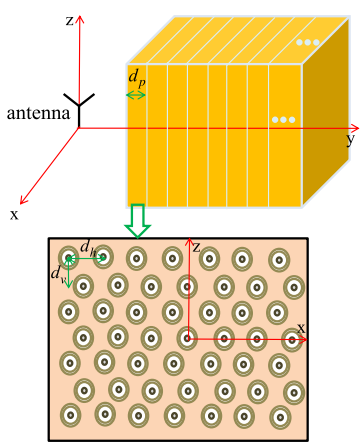

Fig. 14. Three-dimensional model.

top and plane by plane in sequence. In a 3D structure, the cells are connected by multiple scattering. As in the previous analysis, we neglect the weak connections and only keep the forward scattered field which has been proofed to be an efficient way. First, we find the neighbors of a cell which are within the distance d_{nb} from the center of the cell. In the set of the neighbors, we find out the one which is the closest to the antenna. This cell is regarded as the parent of this cell. Once we find the parent for all the cells, we trace back to find the ancestors of each cell. In particular, we find the cell's parent, then we find the parent's parent, so on and so forth until we reach the antenna. Those ancestors are divided into two groups: cells in the near region and cells in the far region. As before, for the near region group we use translational addition theorem, and for the far region group we use plane-wave approximation. Once the scattered field coefficients for each cell is found, we can add the VSWFs to these coefficients and find out the field intensity at any point. The same as previous sections, before adding all the scattered field together, we have to covert the field from different spherical coordinates into a common Cartesian coordinate.

IV. Intra-Body Channel Characteristics

Since the inhomogeneous intra-body environment consists of complicated cells, there are many factors which can affect the field propagation. In this part, we provide the path loss and optimal operating frequency for optical wave in intra-body environment. Then, the effects of antenna radiation, cell position, and layered medium are investigated.

A. Channel Path Loss

In the following analysis, we use path loss as a metric for signal propagation loss. First, we briefly review the path loss definition and introduce the approach we adopted. The received power $P_r(d)$ at a distance d from the transmitting antenna can be approximated by $P_r(d) = P_{ref}(d_0) \cdot \hat{\mathcal{L}}_{ref}(d_0, d)$, where $P_{ref}(d_0)$ is the received power at a close-in reference point in the far field region of the transmitting antenna with distance d_0 [32], and $\hat{\mathcal{L}}_{ref}(d_0, d)$ is the antilogarithm of path loss from d_0 to d. According to [32], by relating power to the electric field radiated by the antenna, the received power $P_r(d)$ can also be expressed by $P_r(d) = |E(d)|^2 A_e/\eta$, where $|E(d)|$ is the electric field intensity at a distance d from the transmitting antenna, A_e is the aperture of the receiving antenna. In the following, we consider the maximum antenna effective aperture that is $3\lambda^2/8\pi$. We can obtain

$$\begin{aligned}\mathcal{L}_{ref}(d_0, d) &= -10 \lg \hat{\mathcal{L}}_{ref}(d_0, d) \\ &= 10 \lg \frac{P_{ref}(d_0)}{P_r(d)} = 20 \lg \frac{|E_{ref}(d_0)|}{|E(d)|}. \end{aligned} \tag{23}$$

The derived path loss $\mathcal{L}_{ref}(d_0, d)$ is based on a reference point d_0. Also, the path loss can be defined as the received power over radiated power ratio. In this way, the antenna's performance is included in the wireless system, which is more practical. The path loss can be updated as

$$\mathcal{L}_{rad}(d) = 10 \lg \frac{P_{rad}}{P_r(d)} = 10 \lg \frac{8\pi^2 \eta^2 |I_0 l|^2}{9|E(d)|^2 \lambda^4}. \tag{24}$$

We set d_0 as a for $\mathcal{L}_{ref}$, and increase the wavelength from 450 nm to 1000 nm gradually. First, to reduce the computation burden, we consider the chain has 20 cells and the mutual intervals are set as $5a$, $7.5a$, and $10a$. As shown in Fig. 15, the wavelength larger than 700 nm suffers from lower loss. As discussed in Section II-C5, the scattering loss is small at long wavelength. Meanwhile the absorption loss is low and it has a minimum value around 700 nm, the scattering loss is much larger than the absorption loss. Therefore, the dominant loss is from scattering. As a result, the longer wavelength has better performance. Also, we can see when using the radiation based path loss, the long wavelength has even lower loss, since the long wavelength antenna has larger antenna aperture thanks to the larger space it occupied to achieve resonance. However, even the results suggest the long wavelength, due to the size constraint in human body, we should strike a balance between the antenna efficiency and antenna size, which is mainly determined by the application.

Next, we increase the number of cells from 5 to 100 with step 5. The interval is kept as $5a$. We consider three wavelengths: 450 nm, 700 nm, and 850 nm. As shown in Fig. 16, in the near region, there is almost no difference for the three wavelengths, since the propagation loss is not obvious. In the far region, the 700 nm and 850 nm achieve much lower path loss than 450 nm. When we consider the radiation power based path loss, the difference is more obvious. Regarding the absorption of blood in different frequencies, we could see that it follows the behavior of hemoglobin rather than cytoplasm, as it can be seen in Fig. 9. The absorption of hemoglobin in our range of study (wavelengths of 450 nm to 1000 nm) is almost four orders of magnitude higher than the values for water and it plays the main absorbing role in blood. Most of existing works are dealing with blood as a homogenous medium. However, when modeling the communication channel between tiny nanomachines floating inside the blood, we consider the blood as a fluid and a couple of obstacles which are the blood cells. The benefit of the model proposed in this paper is that

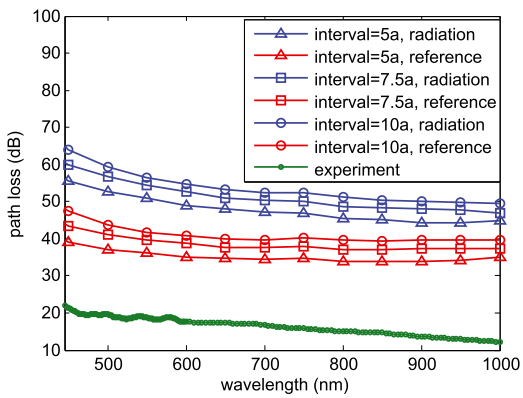

Fig. 15. Path loss for a chain with 20 cells.

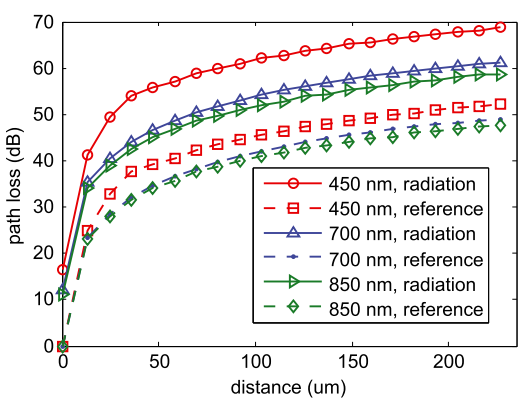

Fig. 16. Path loss for a chain with 100 cells.

it can calculate the field after passing even just one cell which helps model the channel for communication between nanomachines. In that case, the optimal frequency would be around or a little larger than 700 nm as mentioned before in Section II. This is mainly because the transmitter node would emit light inside the cytoplasm, the light passes through a couple of cells and then is being received at the receiver point. Therefore from nanomachines point of view, the EM wave propagates mainly through cytoplasm and on its way to the receiver it observes some obstacles which are mostly red blood cells. Moreover, to be able to see the effect of the cells (in range of micrometers) we should have a wavelength of hundreds of nanometers.

B. Breadth Effect

The plasmonic nanoantenna is small when compared with a cell. Hence, it can only illuminate a small area. As a result, there is no need to consider a large area on a plane. In this part, we gradually increase the number on a plane to see how many we need to consider. In order to investigate the radiation breadth effect of the optical antenna, we keep the plane number as 3 and change the row and column number from 3 to 9 and the step is 2. Then we measure the electric field intensity at $4r_3^m + 1.5a + 2d_p$. The corresponding electric field intensity are 3.32×10^{13} V/m, 2.85×10^{13} V/m, 3.32×10^{13} V/m, and 2.85×10^{13} V/m. The results are almost the same which further proves that the scattering is mostly forward and the impact on adjacent region can be neglected. Hence, in the following analysis, we consider that on each layer there are 3 by 3 cells.

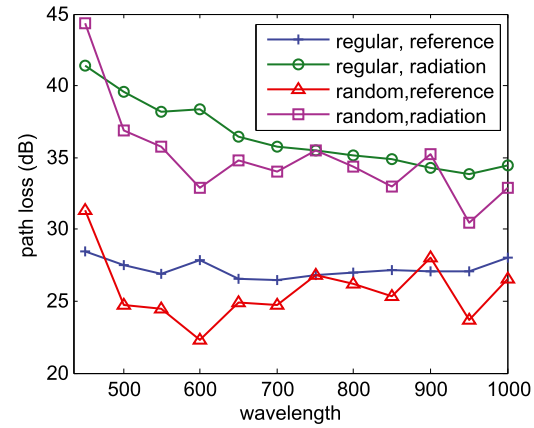

Fig. 17. Three-dimensional model frequency response.

C. Cell Position Effect

In previous discussions, cells' positions are fixed. However, in a more realistic scenario they could be random. In order to investigate the random position effect on optimal frequency, we first find the frequency response of path loss for cells with determined position as shown in Fig. 14 for a comparison. Then we consider the cells have random positions. For the former scenario, the lattice is formed by $3\times3\times5$ cells and the path loss is calculated at (0, $1.5a + 4r_3^m + 4d_p$, 0). The wavelength is gradually changed from 450 nm to 1000 nm with a step 50 nm. As depicted in Fig. 17, the wavelength longer than 700 nm performs better. Note that in three dimensional model, the cells are not on a chain due to the position shift discussed in Section III-C. Also, since we consider the near region, the loss due to propagation is not obvious. Referring to Figs. 4 and 5, the multiple scattering incurs some fluctuations on the magnitude of the electric field intensity. For the radiation power-based path loss, the long wavelength still has better performance due to the antenna's high efficiency.

As shown in Fig. 14, each cell occupies $d_p \cdot d_h \cdot d_v$ space and it is located in the center of a cube since we consider $d_p = d_h = d_v$. Now, we consider the cell's position is no longer fixed and its center's Cartesian coordinates (x_c, y_c, z_c) become $(x_c + \alpha d_p/4, y_c + \alpha d_p/4, z_c + \alpha d_p/4)$, where α is uniformly distributed in (0,1). We set the lattice the same as the regular position case and calculate the mean value of the path loss. As shown in Fig. 17, even if the positions are deviated, the trend of the path loss is still similar. Therefore, even the well aligned model is ideal, and it does not affect the result too much.

D. Field Propagation Among Cells With Layered Structure

All the analyses above consider that the communication range of a plasmonic nanoantenna is very small as well as that all the cells are identical, i.e., exhibit the same properties. However, in real intra-body environment, especially on the boundary of two layers, the cells are quite different in size, structure, material, among many others. Due to the limited space and complicated intra-body environment, we cannot pay our attention to all kinds of cells. However, the developed model in this paper is general. For instance, if the cell only has a single layer (membrane), we find the updated T-matrix for it and follow the same procedure to obtain the results. Furthermore, if the cell size is much larger than what we considered here, we can increase the truncation order N_{stop} to continue the computation.

In Fig. 18, we consider the field propagates in a two-layered structure. Each layer is constructed by 4 planes and on each plane

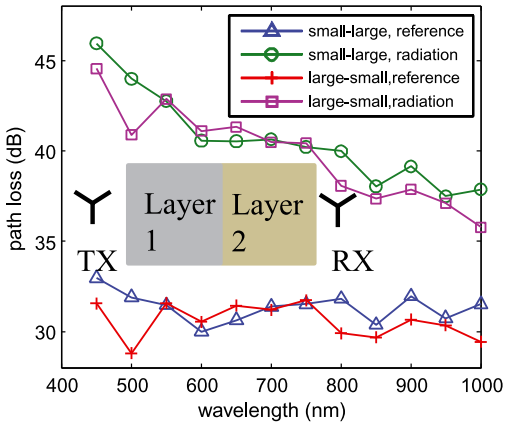

Fig. 18. Path loss in layered structure.

there are 3 by 3 cells whose locations are the same as previous fixed position discussions. First, layer 1 is the large-size cell and layer 2 is the small-size cell. Then, we consider layer 1 is the small-size cell and layer 2 is the large-size cell. The detailed configuration for the two kinds of cells are provided in Table II. As shown in the figure, the wavelength longer than 700 nm still achieves much better performance, especially when we consider the radiated power-based path loss. In addition, there is no significant difference for the propagation direction. The two scenarios have similar performance. When comparing with the result in Fig. 17, the path loss is a little higher. The reason is that the large cells absorbs more power and the electric field experiences more scattering when penetrating the inhomogeneous medium.

V. Conclusions

Nanosensing technology is a promising solution to provide faster and more accurate disease diagnosis and treatment inside the human body. Metallic plasmonic nanoantennas enable wireless communications among intra-body nanodevices at near-infrared and optical frequencies. However, there are several phenomena that challenge the propagation of EM waves inside human body, ranging from the absorption by molecules to the scattering by cells, whose size is comparable to that of the nanodevices. In this paper, a rigorous channel model is developed to understand the intra-body channel behavior as well as to provide insights for the design of iWNSNs. In particular, we have first derived the field intensity distribution around a single cell and analyzed the cell's scattering properties. Then, we extend our discussion to a more realistic scenario with multiple cells. Our models have been validated by means of extensive electromagnetic simulations. The results show that the propagation of EM waves at optical frequencies inside the human body is mainly affected by the scattering from cells. The impact of scattering could be reduced by moving to lower frequencies, i.e., 700 nm to 1000 nm, but this would introduce several challenges. On the one hand, as we reduce the system frequency and approach THz-band frequencies (0.1–10 THz), absorption rapidly increases. Molecular absorption created by internal vibrations of the molecules results into heat, and this is not desirable for intra-body communications. On the other hand, the use of 700 nm to 1000 nm would require the utilization of larger antennas, which would increase the invasiveness and limit the applications of iWNSNs. Communications at 700 nm to 1000 nm within the near-infrared and optical transmission windows can open the door to potentially biocompatible applications of iWNSNs.

Appendix

There are several ways to express vector spherical wave functions (VSWFs) [22], [33]. The VSWFs utilized in this paper can be given by [22],

$$\mathbf{m}_{mn}^{q}(kr,\theta,\phi) = b_n^q(kr) \times \left[\hat{\theta}\frac{jm}{\sin\theta}P_n^m(\cos\theta) - \hat{\phi}\frac{d}{d\theta}P_n^m(\cos\theta)\right]e^{jm\phi}$$

$$\mathbf{n}_{mn}^{q}(kr,\theta,\phi) = \hat{r}\frac{n(n+1)b_n^q(kr)}{kr}P_n^m(\cos\theta)e^{jm\phi} + \frac{b_n^q(kr)+krb_n^{q\prime}(kr)}{kr}\left[\hat{\theta}\frac{d}{d\theta}P_n^m(\cos\theta)+\hat{\phi}\frac{jm}{\sin\theta}P_n^m(\cos\theta)\right]e^{jm\phi}$$

where n is from 1 to ∞, m is from $-n$ to n, and $P_n^m(\cos\theta)$ is the associated Legendre polynomials. The value of q can be 1, 2, or 3, and the corresponding $b_n^q(kr)$ are the first kind of spherical Bessel function $j_n(kr)$, spherical Neumman function $y_n(kr)$, and spherical Hankel function of the second kind $h_n^2(kr)$, respectively.

References

[1] M. A. Eckert and W. Zhao, "Opening windows on new biology and disease mechanisms: Development of real-time *in vivo* sensors," *Interface Focus*, vol. 3, no. 3, p. 20130014, 2013.
[2] I. Akyildiz, M. Pierobon, S. Balasubramaniam, and Y. Koucheryavy, "The internet of bio-nano things," *IEEE Commun. Mag.*, vol. 53, no. 3, pp. 32–40, 2015.
[3] I. F. Akyildiz, F. Brunetti, and C. Blazquez, "Nanonetworks: A new communication paradigm," *Comput. Netw. J.*, vol. 52, no. 12, pp. 2260–2279, Aug. 2008.
[4] M. Pierobon and I. F. Akyildiz, "Capacity of a diffusion-based molecular communication system with channel memory and molecular noise," *IEEE Trans. Inf. Theory*, vol. 59, no. 2, pp. 942–954, 2013.
[5] G. E. Santagati, T. Melodia, L. Galluccio, and S. Palazzo, "Ultrasonic networking for e-health applications," *IEEE Wirel. Commun.*, vol. 20, no. 4, pp. 74–81, 2013.
[6] J. M. Jornet and I. F. Akyildiz, "Graphene-based plasmonic nano-antenna for terahertz band communication in nanonetworks," *IEEE J. Sel. Areas Commun.*, vol. 31, no. 12, pp. 685–694, 2013.
[7] M. Tamagnone, J. S. Gomez-Diaz, J. R. Mosig, and J. Perruisseau-Carrier, "Reconfigurable terahertz plasmonic antenna concept using a graphene stack," *Appl. Phys. Lett.*, vol. 101, no. 21, p. 214102, 2012.
[8] M. Nafari and J. M. Jornet, "Metallic plasmonic nano-antenna for wireless optical communication in intra-body nanonetworks," in *Proc. 10th EAI Int. Conf. Body Area Netw. (BodyNets 2015)*, Sydney, Australia, Sep. 2015.
[9] P. Biagioni, J.-S. Huang, and B. Hecht, "Nanoantennas for visible and infrared radiation," *Rep. Progr. Phys.*, vol. 75, no. 2, p. 024402, 2012.
[10] J. Xu, K. W. Plaxco, and S. J. Allen, "Absorption spectra of liquid water and aqueous buffers between 0.3 and 3.72 THz," *J. Chem. Phys.*, vol. 124, no. 3, 2006, Article no. 036101.
[11] K. Yang, A. Alomainy, and Y. Hao, "In-vivo characterisation and numerical analysis of the THz radio channel for nanoscale body-centric wireless networks," in *Proc. IEEE Radio Sci. Meet. (Joint with AP-S Symp.), 2013 USNC-URSI*, pp. 218–219.
[12] R. M. Pope and E. S. Fry, "Absorption spectrum (380–700 nm) of pure water. ii. integrating cavity measurements," *Appl. Opt.*, vol. 36, no. 33, pp. 8710–8723, 1997.
[13] A. G. Brolo, "Plasmonics for future biosensors," *Nature Photon.*, vol. 6, no. 11, pp. 709–713, 2012.
[14] I. Choi and Y. Choi, "Plasmonic nanosensors: Review and prospect," *IEEE J. Sel. Topics Quantum Electron.*, vol. 18, no. 3, pp. 1110–1121, 2012.
[15] T. P. Ketterl, G. E. Arrobo, A. Sahin, T. J. Tillman, H. Arslan, and R. D. Gitlin, "*In vivo* wireless communication channels," in *Proc. IEEE 13th Annu. Wirel. Microw. Technol. Conf. (WAMICON)*, 2012, pp. 1–3.
[16] L. V. Wang and H.-I. Wu, *Biomedical Optics: Principles and Imaging*. Hoboken, NJ, USA: Wiley, 2007.
[17] J. C. Lin, *Electromagnetic Fields in Biological Systems*. Boca Raton, FL, USA: CRC, 2011.

[18] S. L. Jacques, "Optical properties of biological tissues: A review," *Phys. Med. Biol.*, vol. 58, no. 11, p. R37, 2013.
[19] Q.-H. Park, "Optical antennas and plasmonics," *Contemp. Phys.*, vol. 50, no. 2, pp. 407–423, 2009.
[20] C. A. Balanis, *Antenna Theory: Analysis and Design*. Hoboken, NJ, USA: Wiley, 2005.
[21] M. A. Yurkin, K. A. Semyanov, P. A. Tarasov, A. V. Chernyshev, A. G. Hoekstra, and V. P. Maltsev, "Experimental and theoretical study of light scattering by individual mature red blood cells by use of scanning flow cytometry and a discrete dipole approximation," *Appl. Opt.*, vol. 44, no. 25, pp. 5249–5256, Sep. 2005.
[22] L. Tsang, J. Kong, and K. Ding, *Scattering of Electromagnetic Waves, Theories and Applications*, ser. Wiley Interscience. Hoboken, NJ, USA: Wiley, 2000.
[23] S. Stein, "Addition theorems for spherical wave functions," *Quart. Appl. Math.*, vol. 19, 1961.
[24] D. W. Mackowski, "Analysis of radiative scattering for multiple sphere configurations," *Proc. Roy. Soc. Lond. A, Math. Phys. Sci.*, vol. 433, no. 1889, pp. 599–614, 1991.
[25] J. Shen, "Algorithm of numerical calculation on lorentz mie theory," *PIERS Online*, vol. 1, no. 6, pp. 691–694, 2005.
[26] S. Smye, J. Chamberlain, A. Fitzgerald, and E. Berry, "The interaction between terahertz radiation and biological tissue," *Phys. Med. Biol.*, vol. 46, no. 9, p. R101, 2001.
[27] R. L. van Veen, H. Sterenborg, A. Pifferi, A. Torricelli, and R. Cubeddu, "Determination of VIS-NIR absorption coefficients of mammalian fat, with time-and spatially resolved diffuse reflectance and transmission spectroscopy," in *Opt. Soc. Amer. Biomed. Topical Meet.*, Miami Beach, FL, USA, 2004, Article no. SF4.
[28] S. Prahl, 1999, Oregon Medical Laser Center [Online]. Available: http://omlc.org/spectra/hemoglobin/summary.html
[29] N. Bosschaart, G. J. Edelman, M. C. Aalders, T. G. van Leeuwen, and D. J. Faber, "A literature review and novel theoretical approach on the optical properties of whole blood," *Lasers Med. Sci.*, vol. 29, no. 2, pp. 453–479, 2014.
[30] J. R. Mourant, J. Boyer, A. H. Hielscher, and I. J. Bigio, "Influence of the scattering phase function on light transport measurements in turbid media performed with small source-detector separations," *Opt. Lett.*, vol. 21, no. 7, pp. 546–548, 1996.
[31] L. Tsang and J. A. Kong, *Scattering of Electromagnetic Waves, Advanced Topics*. Hoboken, NJ, USA: Wiley, 2004, vol. 26.
[32] T. S. Rappaport *et al., Wireless Communications: Principles and Practice*. Upper Saddle River, NJ, USA: Prentice-Hall, 1996, vol. 2.
[33] J. Stratton, I. Antennas, and P. Society, *Electromagnetic Theory*, ser. IEEE Press Classic Reissue. Piscatawat, NJ, USA: Wiley, 2007.

Hongzhi Guo (S'12) received his B.S. degree in Automation from Shandong University of Science and Technology, Qingdao, China, in 2011 and M.S. degree in Electrical Engineering from Columbia University, New York, in 2013. Currently, he is working toward the Ph.D. degree in the Electrical Engineering Department at State University of New York, Buffalo, NY, USA, under guidance of Prof. Zhi Sun. His current research interests are in wave propagation in complex environments, antenna design, metamaterial modeling, and wireless channel modeling.

Pedram Johari (S'11) received the B.S. degree in electrical engineering (electronics) from Islamic Azad University Central Tehran Branch, Tehran, Iran, and the M.S. degree in electrical engineering (communication systems) from Iran University of Science and Technology, Tehran, Iran, in 2006 and 2012, respectively. He is currently working toward the Ph.D. degree in the Department of Electrical Engineering at the University at Buffalo, State University of New York, Buffalo, NY, USA. He was the recipient of the Outstanding Graduate Student Award, for outstanding academic achievements in the Department of Electrical Engineering, University at Buffalo, in 2015. His current research interests are in terahertz band communication networks and electromagnetic nanonetworks.

Josep Miquel Jornet (M'13) received the Engineering degree in telecommunication and the M.Sc. degree in information and communication technologies from the Universitat Politecnica de Catalunya, Barcelona, Spain, in 2008. He received the Ph.D. degree in electrical and computer engineering from the Georgia Institute of Technology, Atlanta, GA, USA, in 2013, with a fellowship from "la Caixa" (2009–2010) and Fundacion Caja Madrid (2011–2012). He is currently an Assistant Professor with the Department of Electrical Engineering at the University at Buffalo, State University of New York, Buffalo, NY, USA. From September 2007 to December 2008, he was a visiting researcher at the Massachusetts Institute of Technology (MIT), Cambridge, MA, USA, under the MIT Sea Grant program. He was the recipient of the Oscar P. Cleaver Award for outstanding graduate students in the School of Electrical and Computer Engineering, at the Georgia Institute of Technology, Atlanta, GA, USA, in 2009. He also received the Broadband Wireless Networking Lab Researcher of the Year Award at the Georgia Institute of Technology in 2010. He is a Member of the ACM. His current research interests are in terahertz-band communication networks, nanophotonic wireless communication, graphene-enabled wireless communications, electromagnetic nanonetworks, intra-body wireless nanosensor networks and the Internet of Nano-Things.

Zhi Sun (M'11) received the B.S. degree in telecommunication engineering from Beijing University of Posts and Telecommunications (BUPT), Beijing, China, the M.S. degree in electronic engineering from Tsinghua University, Beijing, China, in 2004 and 2007, respectively, and the Ph.D. degree in electrical and computer engineering from Georgia Institute of Technology, Atlanta, GA, USA, in 2011. Currently, he is an Assistant Professor with the Department of Electrical Engineering, State University of New York at Buffalo, Buffalo, NY, USA. Prior to that, he was a Postdoctoral Fellow with Georgia Institute of Technology, Atlanta, GA, USA. Prof. Sun was the recipient of the Best Paper Award in the 2010 IEEE Global Communications Conference (Globecom). He was also the recipient of the BWN Researcher of the Year Award at Georgia Institute of Technology in 2009, and the Outstanding Graduate Award at Tsinghua University, China, in 2007. His research interests include wireless communication and networking in complex environments, metamaterial enhanced communication and security, wireless intra-body networks, wireless underground networks, wireless underwater networks, and cyber physical systems.